

THE EFFECT OF ANISOTROPIC CONDUCTION ON THE THERMAL INSTABILITY IN THE INTERSTELLAR MEDIUM

ENA CHOI & JAMES M. STONE

Department of Astrophysical Sciences, Princeton University, Princeton, NJ 08544

Draft version May 5, 2017

ABSTRACT

Thermal instability (TI) can strongly affect the structure and dynamics of the interstellar medium (ISM) in the Milky Way and other disk galaxies. Thermal conduction plays an important role in the TI by stabilizing small scales and limiting the size of the smallest condensates. In the magnetized ISM, however, heat is conducted anisotropically (primarily along magnetic field lines). We investigate the effects of anisotropic thermal conduction on the nonlinear regime of the TI by performing two-dimensional magnetohydrodynamic simulations. We present models with magnetic fields of different initial geometries and strengths, and compare them to hydrodynamic models with isotropic conduction. We find anisotropic conduction does not significantly alter the overall density and temperature statistics in the saturated state of the TI. However, it can strongly affect the shapes and sizes of cold clouds formed by the TI. For example, for uniform initial fields long filaments of cold gas are produced that are reminiscent of some observed HI clouds. For initially tangled fields, such filaments are not produced. We also show that anisotropic conduction suppresses turbulence generated by evaporative flows from the surfaces of cold blobs, which may have implications for mechanisms for driving turbulence in the ISM.

Subject headings: galaxies: ISM – instabilities – ISM: kinematics and dynamics

1. INTRODUCTION

The thermal instability (TI) plays an important role in controlling several different aspects of the interstellar medium (ISM) and star formation. For example, it has been invoked to explain the observed multiphase structure of the ISM (Parker 1953; Spitzer 1958; Field 1965; Field, Goldsmith, & Habing 1969). The linear stage of the TI in astrophysical gases was first studied in detail by Field (1965). He identified three unstable modes: an isobaric and two isentropic modes. In the nonlinear regime, the isobaric mode produces condensations that are fundamental to the classical two-phase model of the ISM (Field, Goldsmith, & Habing 1969), as well as the extension to a three-phase model by Cox & Smith (1974); Mckee & Ostriker (1977). The TI also regulates the mass flow between the different components of the ISM, and therefore affects the star formation rate (Chiéze 1987). Thus, it is important to investigate the role of TI in determining the distribution of density, temperature, and other physical variables in the multiphase ISM. For this reason, a variety of authors have studied the linear and nonlinear stages of the TI using numerical hydrodynamic simulations (Hennebelle & Pérault 1999; Kritsuk & Norman 2002a,b, 2004; Vázquez-Semadeni, Gazol, & Scalo 2000; Gazol et al. 2001; Sánchez-Salcedo, Vázquez-Semadeni & Gazol 2002; Piontek & Ostriker 2004, 2005; Koyama & Inutsuka 2004; Vázquez-Semadeni et al. 2007; Kim, Kim, & Ostriker 2008; Inoue & Inutsuka 2008).

Thermal conduction is important to include in studies of the TI for two reasons. First, it suppresses the growth rate at small scales, in fact isobaric perturbations with wavelength smaller than the Field length λ_F (Field 1965) do not grow at all. Second, it produces evaporation from the surfaces of cold dense fragments, and the interaction of the evaporative flows can induce turbulence.

Including thermal conduction is essential for numerical studies of the TI. Without explicit thermal conduction, perturbations at the grid scale grow fastest, and may even-

tually come to dominate the dynamics. For this reason, Koyama & Inutsuka (2004) concluded that numerical studies of the TI must satisfy a "Field criterion", that is the Field length must be resolved by at least a few cells to prevent artificial fragmentation at the grid scale, and to avoid the results being dominated by grid noise. Satisfying the Field criterion requires including explicit thermal conduction (Piontek & Ostriker 2004, 2005; Koyama & Inutsuka 2004; Brandenburg, Korpi & Mee 2007). To highlight one example, Piontek & Ostriker (2004, 2005) studied the interaction of the TI and the magnetorotational instability (MRI) in disks including isotropic thermal conduction; they found the MRI could drive turbulence and fragmentation in the diffuse ISM at amplitudes consistent with HI observations.

To date most studies of the TI with conduction have assumed the conductivity is isotropic. However, in a magnetized plasma, electrons can flow more freely along magnetic field lines than across them, leading to anisotropic transport coefficients (Spitzer 1962). The degree of anisotropy is measured by the ratio of the electron gyro radius to the mean free path between collisions. For the warm medium, where typically $T = 1500$ K, $n = 2$ cm³, and $B = 1\mu$ G, the Columb mean free path is $\lambda_{\text{mfp}} \sim 10^{10}$ cm, while the electron gyro radius is $r_g = 10^6$ cm. Thus, in this medium the thermal conduction should be highly anisotropic, and primarily along magnetic field lines.

The implications of anisotropic transport terms on the dynamics of astrophysical plasmas has begun to be explored recently (Balbus 2001; Sharma, Hammett & Quataert 2003; Parrish & Stone 2005). For example, in stratified atmospheres, anisotropic conduction can result in the magnetothermal and heat-flux buoyancy instabilities in the intracluster medium (Parrish & Stone 2008; Sharma et al. 2009). In addition, it can have effects on the evolution of supernova remnants (Balsara, Tilley & Howk 2008) and on magnetized spherical accretion flows (Sharma, Quataert & Stone 2008). Recently, Sharma, Parrish & Quataert (2010) studied the TI

in the intracluster medium, including heating by cosmic rays. Their primary result is that with anisotropic thermal conduction, the TI could produce filaments of cold gas orientated along magnetic field lines.

In this study, we perform two-dimensional numerical hydrodynamic and magnetohydrodynamic simulations of TI in the ISM that include the anisotropic heat conduction. The purpose of this paper is to investigate the effects of anisotropic thermal conduction on the structure and dynamics of interstellar medium, and to compare the results to models which include only isotropic conduction. Since the geometry and strength of magnetic field in different regions of the ISM may vary, we perform simulations of the TI with various magnetic field strengths and two different initial geometries for the field.

Ideally, the numerical studies of the thermal instability should include both isotropic and anisotropic conduction with the temperature dependency since the thermal instability develops density distribution with distinct peaks in the cold/dense phase dominated by isotropic conduction and in the diffuse/hot phase with higher ionization fraction and thus more affected by anisotropic conduction. However, including both isotropic and anisotropic conduction with a realistic temperature dependency is challenging, since it would decrease the Field length, and require higher resolution. In this study, we restrict our exploration to the simulations only with isotropic conduction or ones only with anisotropic conduction to better understand the effects of anisotropic conduction.

This paper is organized as follows: our numerical methods and code tests are summarized in § 2. In § 3, we first discuss the effects of the conduction rate and resolution on the TI in hydrodynamical simulations, and then use these results to choose a specific set of model parameters for our simulations. Results from calculations of the nonlinear regime of the TI with anisotropic conduction are presented in § 4. We summarize and discuss our results in § 5.

2. NUMERICAL MODEL

We solve the equations of ideal MHD with additional terms for radiative cooling, heating, and heat conduction

$$\frac{\partial \rho}{\partial t} + \nabla \cdot [\rho \mathbf{v}] = 0, \quad (1)$$

$$\frac{\partial \rho \mathbf{v}}{\partial t} + \nabla \cdot \left[\rho \mathbf{v} \mathbf{v} - \mathbf{B} \mathbf{B} + \left(p + \frac{B^2}{2} \right) \mathbf{I} - \boldsymbol{\sigma} \right] = 0, \quad (2)$$

$$\frac{\partial E}{\partial t} + \nabla \cdot \left[\left(E + p + \frac{B^2}{2} \right) \mathbf{v} - \mathbf{B} (\mathbf{B} \cdot \mathbf{v}) + \mathbf{Q} - \mathbf{v} \cdot \boldsymbol{\sigma} \right] = -\rho \mathcal{L}, \quad (3)$$

$$\frac{\partial \mathbf{B}}{\partial t} - \nabla \times (\mathbf{v} \times \mathbf{B}) = 0, \quad (4)$$

where the symbols have their usual meaning. The total energy density E is given as

$$E = \frac{P}{\gamma - 1} + \frac{1}{2} \rho v^2 + \frac{B^2}{2}, \quad (5)$$

where γ is the ratio of specific heats (assumed to be 5/3 throughout this paper). Here, $\boldsymbol{\sigma}$ is the viscous stress tensor

$$\sigma_{ij} = \eta \left[\left(\frac{\partial \mathbf{v}_i}{\partial x_j} + \frac{\partial \mathbf{v}_j}{\partial x_i} \right) - \frac{2}{3} \delta_{ij} \nabla \cdot \mathbf{v} \right] \quad (6)$$

where η is the coefficient of viscosity and summation over repeated indices is implied. In equation 3, \mathbf{Q} denotes the heat

flux and $\mathcal{L} = \rho \Lambda(\rho, T) - \Gamma$ is the net cooling function, where $\Lambda(\rho, T)$ and Γ are the cooling and heating rates per unit mass respectively. These equations are written in units such that the magnetic permeability $\mu_B = 1$.

The heating and cooling rates are

$$\mu m_H \Gamma = 2 \times 10^{-26} \text{ erg s}^{-1}, \quad (7)$$

$$\begin{aligned} \mu m_H \frac{\Lambda(T)}{\Gamma} &= 10^7 \exp \left(\frac{-1.184 \times 10^5}{T + 1000} \right) \\ &+ 1.4 \times 10^{-2} \sqrt{T} \exp \left(\frac{-92}{T} \right) \text{ cm}^3 \end{aligned} \quad (8)$$

where we have adopted the functional fit to the ISM cooling rates as suggested by Koyama & Inutsuka (2002)¹. For the net cooling curve adopted in this work, the transition temperatures that define the warm (phase "F", $T > T_{\text{max}}$), intermediate (phase "G", $T_{\text{min}} < T < T_{\text{max}}$), and cold (phase "H", at $T < T_{\text{min}}$) phases are $T_{\text{max}} = 5012$ K and $T_{\text{min}} = 185$ K respectively.

In the case of *isotropic* conduction, the heat flux \mathbf{Q} is given by

$$\mathbf{Q} = \mathbf{Q}_{\text{iso}} = -\mathcal{K} \nabla T, \quad (9)$$

while in the case of *anisotropic* conduction, the heat flux is given by

$$\mathbf{Q} = \mathbf{Q}_{\text{aniso}} = -\mathcal{K} \hat{\mathbf{b}} \hat{\mathbf{b}} \cdot \nabla T. \quad (10)$$

where $\hat{\mathbf{b}}$ is a unit vector in the direction of the magnetic field, and \mathcal{K} is the conductivity. For the temperature ranges considered here, the latter is given by (Parker 1953; Spitzer 1962)

$$\mathcal{K} = 2.5 \times 10^3 T^{1/2} \text{ erg cm}^{-1} \text{ K}^{-1} \text{ s}^{-1}. \quad (11)$$

The relation between the dynamic viscosity coefficient η and the thermal conductivity \mathcal{K} can be characterized by the Prandtl number:

$$\text{Pr} = \frac{\gamma}{\gamma - 1} \frac{k_B}{m_H} \frac{\eta}{\mathcal{K}}. \quad (12)$$

The Prandtl number for a neutral monoatomic gas is $\text{Pr} = 2/3$. For most of the simulations presented in this paper, we include explicit viscosity with a constant coefficient of viscosity that corresponds to a Prandtl number $\text{Pr} = 2/3$.

All of the numerical results presented in this paper were calculated using Athena. Details of the algorithms implemented in Athena are documented in Gardiner & Stone (2005, 2008) and extensive tests of the MHD algorithms in Athena are shown in Stone et al. (2008). In this work, we use the Roe approximate Riemann solver and the directionally unsplit CTU (corner transport upwind) integration scheme. Optically thin cooling was added to the integrators without using operator splitting. To circumvent timestep constraints in regions of strong cooling, we limit the minimum temperature to the equilibrium value where heating balances cooling. This allows large time steps while avoiding the large errors or overshoots encountered with backward Euler or Crank-Nicholson implicit differencing.

We solve the equations in a rectangular domain with periodic boundary conditions and no gravity. Our domain spans a

¹ Equation 8 contains the corrections pointed out by Nagashima, Inutsuka & Koyama (2006)

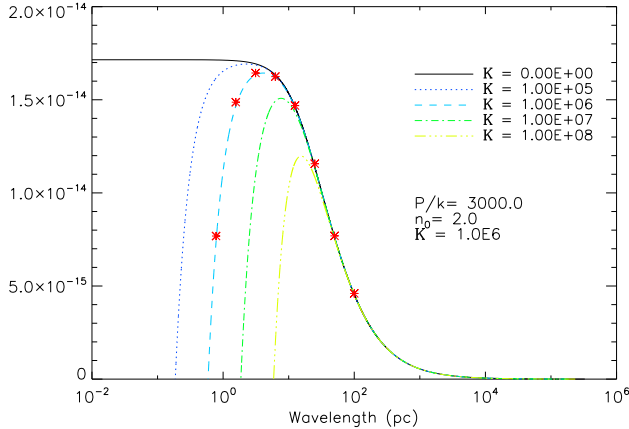


FIG. 1.— Numerically measured growth rates of the TI for different wave numbers and with a constant conductivity $\mathcal{K} = 10^6 \text{ erg cm}^{-1} \text{ K}^{-1} \text{ s}^{-1}$ plotted as points, overlaid with the theoretical growth rates for conductivities of $\mathcal{K} = [0.0, 10^5, 10^6, 10^7, 10^8] \text{ erg cm}^{-1} \text{ K}^{-1} \text{ s}^{-1}$. The excellent agreement between the numerical and analytic growth rates verifies our numerical algorithms.

region of size $2L \times L$, where L is varied between different calculations. We adopt an initial pressure of $P/k = 3000 \text{ K cm}^{-3}$ and density of $n = 2.0 \text{ cm}^{-3}$. The equilibrium pressure corresponding to this density is $P/k = 2896.6 \text{ K cm}^{-3}$, so our initial condition is in a slowly cooling state. The mean mass per particle in units of the mass of atomic hydrogen is $\mu = 1.27$, representing 10% He abundance by number. To initiate the thermal instability (TI), we add random pressure perturbations with a maximum amplitude of 0.1%. For our assumed initial temperature, the fiducial value of the conductivity is

$$\mathcal{K}_0 = 9.68 \times 10^4 \text{ erg cm}^{-1} \text{ K}^{-1} \text{ s}^{-1} \quad (13)$$

which follows from equation 11.

In order to test the implementation of the heating, cooling and conduction terms in our code, we have performed one-dimensional simulations of the TI, and compared the numerically measured growth rates with the theoretical prediction Field (1965). The initial conditions for this test are a medium at rest with constant density and pressure of $n = 2.0 \text{ cm}^{-3}$ and $P/k = 3000 \text{ K cm}^{-3}$, and isotropic conduction with coefficient $\mathcal{K} = 10^6 \text{ erg s}^{-1} \text{ cm}^{-1} \text{ K}^{-1}$. The box size was $L = 100 \text{ pc}$ and the grid contained 1024 zones. We initialize the models with eigen modes of the instability by imposing sinusoidal fluctuations of amplitude 1 percent and with wave number k , and measure the growth rate of the density for different values of k . Figure 1 compares the numerical growth rates from our simulations along with the theoretical values using four values of the thermal conductivity \mathcal{K} . Clearly there is good agreement between the analytic and numerical growth rates; the numerical method reproduces the theoretical value of the growth rate to better than 4 percent in all cases.

For any non-zero value of the conductivity, the thermal diffusivity becomes comparable to the heating and cooling term at a critical wavelength referred to as the Field length, given approximately by Field (1965)

$$\lambda_F = 2\pi \sqrt{\frac{\mathcal{K}T}{\rho^2 \Lambda}}. \quad (14)$$

In the case of no conduction $\mathcal{K} = 0$, the growth rate of the TI is largest at the smallest scales ($\lambda = 0$). For this reason,

TABLE 1
MODELS WITH ISOTROPIC CONDUCTION.

Conductivity	$\lambda_F^a / \lambda_{F,min}$	Box size (pc)	$n_{\lambda_F}^b$	$\Delta x(\text{pc})$	$n_c^c / n_{c,min}$
0.0	-	4.0×2.0	-	0.00195	-
\mathcal{K}_0	0.12 / 0.006	4.0×2.0	33.3	0.00195	61.5 / 3
$4\mathcal{K}_0$	0.24 / 0.012	8.0×4.0	33.3	0.0039	61.5 / 3
$16\mathcal{K}_0$	0.48 / 0.024	16.0×8.0	33.3	0.0078	61.5 / 3
$64\mathcal{K}_0$	0.96 / 0.048	32.0×16.0	33.3	0.0156	61.5 / 3

^aField length in parsec as given by Equation 14.

^bThe number of Field lengths along the longest axis of the simulation box ($2L$).

^cField number, i.e., the number of zones in a Field length.

Koyama & Inutsuka (2004) have shown that the inclusion of explicit thermal conduction is necessary in studies of the TI in order to damp growth at the grid scale and ensure the fastest growing modes of the TI Field (1965) are resolved by at least three cells. Without explicit conduction, grid noise will be amplified until it dominates the solution. We further investigate the consequences of simulating the TI without explicit thermal conduction in the next section.

3. TI WITH ISOTROPIC THERMAL CONDUCTION

In the following subsections, we investigate the role of varying the amplitude of the conductivity, size of the computational domain, and grid resolution using models with isotropic conduction. This allows us to decide on an optimal set of model parameters before considering the effect of anisotropic conduction in the next section.

3.1. Effect of varying the conductivity

With our adopted initial condition of density and temperature and with the standard level of thermal conduction \mathcal{K}_0 , the Field length λ_F is about 0.12 pc. Resolving this length in a computational domain that spans hundreds of parsecs is very demanding. Thus, in most previous work, the thermal conductivity has either been increased (by about a factor of 100) in order to resolve the Field length (Piontek & Ostriker 2004, 2005; Brandenburg, Korpi & Mee 2007), or the computational domain has been chosen to be very small (for example 0.3–4.8pc) Koyama & Inutsuka (2004, 2006) so that the standard value \mathcal{K}_0 can be used. In this section, we study whether the properties of the nonlinear regime of the TI depend on the value of the conductivity adopted.

We present the results of five inviscid hydrodynamical models which include isotropic conduction with values for the conductivity of $\mathcal{K} = [0.0, \mathcal{K}_0, 4\mathcal{K}_0, 16\mathcal{K}_0, 64\mathcal{K}_0]$. Table 1 summarizes the properties of the simulations.

Each model begins from a uniform homogeneous medium at rest with the fiducial density and pressure. Each uses the same numerical resolution, 2048×1024 cells, but the size of the domain L is varied so that the Field length is resolved, even in the nonlinear regime. Since the Field length is proportional to \sqrt{T} and inversely proportional to density n , as density inhomogeneities are amplified by the TI the local value of the Field length varies, i.e., the local Field length in the regions of hot gas increases and that in regions of cold gas decreases. By the end of the simulation, we find the Field length in the cold gas is ~ 20 times smaller than in the initial conditions. To fully resolve the Field length throughout the simulation, grid cells must be smaller than the Field length *in the cold phase*. We calculate the minimum value of the Field length $\lambda_{F,min}$ for

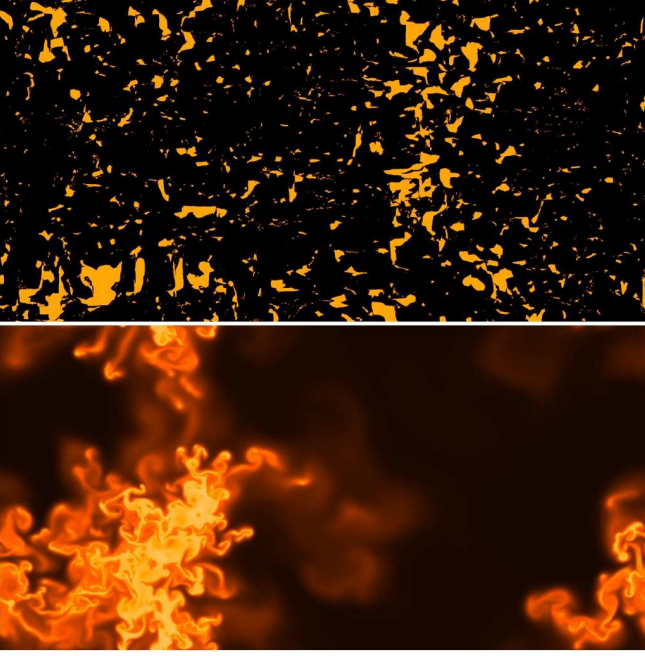


FIG. 2.— Density snapshots at $t \sim 200$ Myr for the inviscid TI simulations without thermal conduction (top) and with isotropic uniform conduction of $\mathcal{K} = \mathcal{K}_0$ (bottom). A logarithmic color scale from $n = 0.28 \text{ cm}^{-3}$ to $n = 170 \text{ cm}^{-3}$ is used.

cold gas and keep the Field number $n_c = \lambda_F / \delta x$, greater than 3 throughout our simulations.

We choose the physical size of the domain L to be large enough so that it spans a large number of Field lengths, similar to the value used in previous work (Piontek & Ostriker 2004, 2005; Brandenburg, Korpi & Mee 2007). Defining n_{λ_F} as the number of Field lengths along the longest axis of the simulation box ($2L$), we vary L so that for each value of the conductivity, n_{λ_F} is fixed. We have also performed a large number of simulations with the same conductivity \mathcal{K} but different values of L to confirm that the statistical properties of the density and the level of kinetic energy in the nonlinear stage of the TI are not affected by changing L (provided that n_{λ_F} is large). Thus, we are confident we can compare runs with different physical sizes to isolate the effect of varying the conductivity on the TI.

Figure 2 plots the density at $t \sim 200$ Myr in two models: a calculation without conduction ($\mathcal{K} = 0$, top) and one with $\mathcal{K} = \mathcal{K}_0$ (bottom). Density structures formed by the TI are significantly different between the two models. In the case of no thermal conduction (top panel), very small dense and cold fragments begin to form at the beginning of the simulation. These fragments are unresolved (1-2 cells in size). As time proceeds they begin to merge, and by the end of the calculation at 200 Myr, they dominate the results. On the other hand, for the simulation with $\mathcal{K} = \mathcal{K}_0$ (bottom panel), resolved density structures begin to emerge at about 20 Myr, and continue to grow into a network of filaments that forms by about 25 Myr. By ~ 33 Myr, dense cold clouds in thermal equilibrium form. The shape and size of the cold clouds evolves due to evaporation and winds driven from their surfaces by thermal conduction. The smallest clouds evident in the density figure have a short lifetime (less than ~ 2 Myr), as they are quickly dissolved by evaporation, and continuously reformed by the evolving density structures.

Figure 3 shows the mass-weighted density PDFs for the

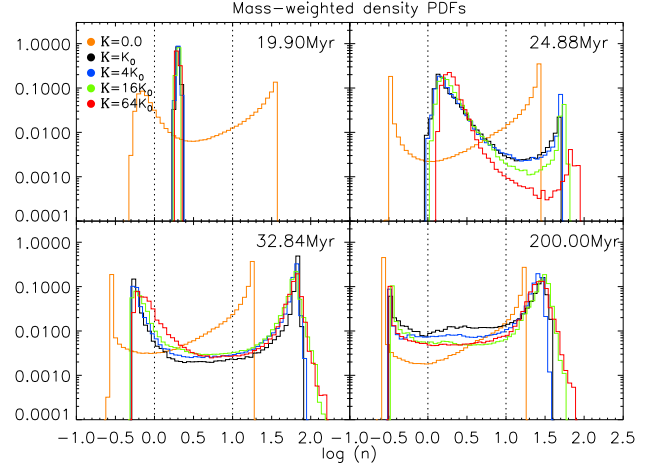


FIG. 3.— Mass weighted density PDFs for inviscid TI simulations with different values of an isotropic conductivity at $t \sim 20, 25, 33, 200$ Myr.

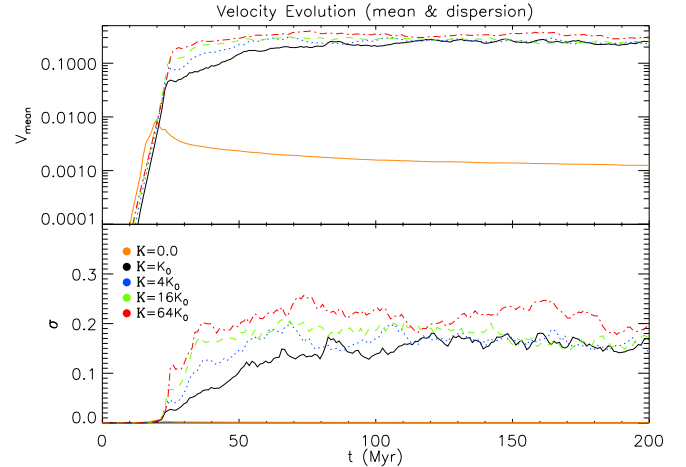


FIG. 4.— Mass weighted mean velocity (top) and velocity dispersion (bottom) of inviscid TI models with different values of an isotropic conductivity as a function of time.

five models with different level of thermal conductivity. At $t = 20$ Myr, all the gas in the models with thermal conduction are in the unstable regime, however in the model without conduction the density is already segregated into two phases. Not until $t = 33$ Myr do the models with conduction form density distributions that are clearly separated into two distinct phases. After this time, the shape and size of dense clouds evolve due to condensation, evaporation, and thermal winds as shown in Figure 2, so that there are always some fraction of the gas in the interface regions that is in the thermally unstable regime. The mass of gas in the unstable regime *increases* as the value of the conductivity increases. Moreover, the highest density also *increases* with the value of the conductivity.

In Figure 4, we plot the mass-weighted mean velocity, defined as $\bar{v} \equiv \sqrt{\langle \rho v^2 \rangle / \langle \rho^2 \rangle}$, and the velocity dispersion for each of the five models. In each case the velocity dispersion increases rapidly by TI-induced turbulence. Without thermal conduction (orange solid line), the velocity dispersion and average velocity attain their maximum values by $t \sim 20$ Myr. In contrast, in the models with thermal conduction, the velocity dispersion and the average velocity keep increasing because of the continuous supply of unstable gas produced by thermal evaporation from the surfaces of dense clouds as discussed in Inoue, Inutsuka & Koyama (2006). Thus, the

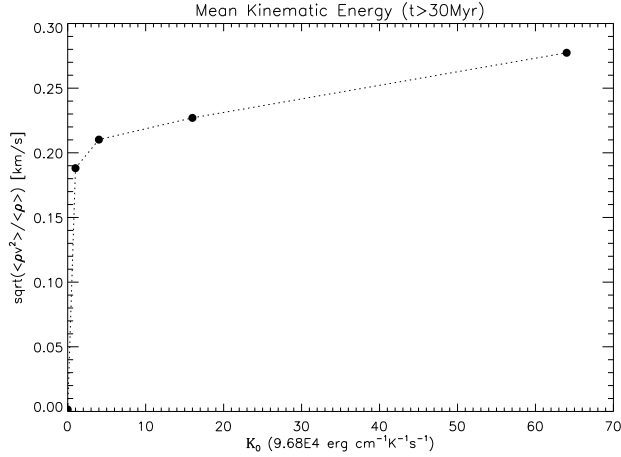


FIG. 5.— The saturated velocity as a function of isotropic thermal conductivity.

model without thermal conduction (orange solid line) has the smallest values of both the average velocity and velocity dispersion, while the model that includes the highest level of conductivity (red dotted line) has the largest.

The mass-weighted mean velocity calculated at $t \geq 50$ Myr as a function of the thermal conductivity is shown in Figure 5. Clearly the amplitude of the turbulence induced by thermal instability increases in proportion to the value of the thermal conductivity, at least for $\mathcal{K} > \mathcal{K}_0$.

We draw two conclusions from this study. First, as has already been shown in many recent studies (Koyama & Inutsuka 2004; Piontek & Ostriker 2004), we conclude it is critically important to include explicit thermal conduction in simulations of the TI. Figure 2 dramatically demonstrates how calculations without conduction lead to unresolved fragments that do not evaporate or drive turbulence. Figure 3 shows the substantial differences between the PDF of the density in models that include conduction, in comparison to a model that does not. Any study of TI-driven turbulence in the ISM that does not include conduction will be dominated by errors seeded by the grid. Second, we conclude it is important to adopt the appropriate value for the conductivity. Adopting a larger value in order to resolve the Field length results in overestimating the level of turbulence driven by evaporative flows, and modifies the PDF of the density.

3.2. Effect of numerical resolution and viscosity

Based on the results from the previous subsection, in the remainder of this paper we present models in which the conductivity $\mathcal{K} = \mathcal{K}_0$. The corresponding Field length is $\lambda_F = 0.12$ pc. Based on one dimensional simulations, Koyama & Inutsuka (2004) have shown that the Field number $n_c = \lambda_{F,min} / \delta x$ should be greater than 3 to achieve convergence in the number of clouds formed by the TI, and the maximum Mach number at late time in their simulations. It is important to confirm that convergence is achieved if the Field length is resolved in our two dimensional study. Therefore we have run inviscid simulations of the TI with isotropic conduction with three different numerical resolutions: 1024×512 (low resolution), 2048×1024 (standard resolution), and 4096×2048 (high resolution). All models are computed in a domain of size $2L \times L$, where $L = 2$ pc. We have also run models with a constant coefficient of dynamic viscosity corresponding to a Prandtl number $\text{Pr} = 2/3$ at all three resolutions.

Figure 6 shows the density PDFs at $t \sim 150$ Myr both for

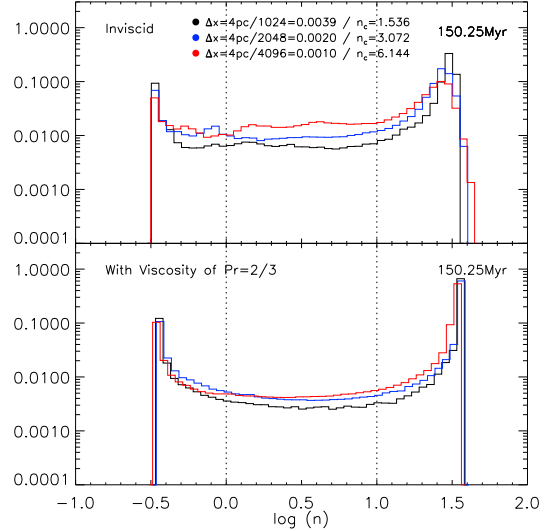


FIG. 6.— Mass weighted density PDFs at $t \sim 150$ Myr in models computed with different resolutions. (Top) Density PDFs of inviscid models. (Bottom) Density PDFs of models with explicit viscosity and $\text{Pr} = 2/3$.

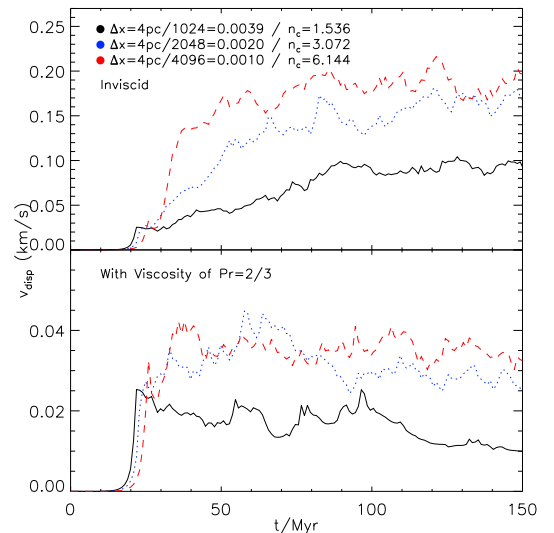


FIG. 7.— Mass weighted velocity dispersion as a function of time at different numerical resolutions for inviscid calculations (top), and calculations with explicit viscosity and $\text{Pr} = 2/3$.

inviscid models and models with viscosity at different resolutions. The PDF of the inviscid calculations (*top panel*) are resolution dependent, especially for the maximum density and the amount of mass in the unstable regime. The highest resolution inviscid model shows the largest value of the maximum density reached in cold gas, and has a much larger amount of matter in the unstable regime compared to lower resolutions. The latter is a reflection of the fact that matter in the unstable regime is contained in dynamical regimes that are driven by thermal evaporation, and the properties of these evaporative flows are affected by viscosity. The bottom panel of Figure 6 shows that both the maximum value of the density and the amount of matter in the unstable regime converge with resolution if explicit viscosity is included. In this case, the mass-weighted fraction of matter in the unstable regime is 5.8, 8.2, 9.0 % for the low, standard, and high resolution models respectively.

TABLE 2
MODELS WITH ANISOTROPIC CONDUCTION

Model	Conduction	Viscosity	Magnetic Field	β
1	hydro/Isotropic	inviscid	-	-
2	mhd/Anisotropic	inviscid	uniform	10^6
3	mhd/Anisotropic	inviscid	uniform	1
4	mhd/Anisotropic	inviscid	tangled	10^6
5	mhd/Anisotropic	inviscid	tangled	1
6	hydro/Isotropic	Pr = 2/3	-	-
7	mhd/Anisotropic	Pr = 2/3	uniform	10^6
8	mhd/Anisotropic	Pr = 2/3	uniform	1
9	mhd/Anisotropic	Pr = 2/3	tangled	10^6
10	mhd/Anisotropic	Pr = 2/3	tangled	1

Figure 7 shows the mass-weighted velocity dispersion as a function of time at different numerical resolutions for models both with and without explicit viscosity. In all the models, the velocity dispersion starts to rapidly increase at around $t \sim 20$ Myr, when dense structures begin to form (see also Figures 2 and 3). While the velocity dispersion of the inviscid models continues to increase until $t \sim 50$ Myr, in the models with explicit viscosity it remains relatively constant after turbulence initially develops. In either case, the velocity dispersion saturates after $t \sim 50$ Myr, however the mean velocity in the saturated state of the inviscid models is almost 5 times larger than those that include explicit viscosity. Specifically, for $t \geq 50$ Myr the mass-weighted mean velocity in the inviscid models with low, standard, and high resolution is 0.10, 0.19, 0.24 km/s respectively, while models with viscosity have mean velocities that are only 0.017, 0.037, 0.043 km/s. This difference is likely due to the fact that the inviscid models have 2–3 times more matter in the unstable regime, which drives correspondingly more powerful evaporative flows. The highest resolution model with viscosity has only a 15% larger mean velocity in the saturated state than that of the standard resolution model, which is further evidence all quantities are converging.

Based on these convergence tests, we conclude that some properties of the nonlinear regime of the TI with isotropic conduction are still resolution dependent even if the Field length is well resolved if explicit viscosity is not included. For this reason, in studies with anisotropic conduction presented in the next section, we will present results both with and without viscosity.

4. TI WITH ANISOTROPIC THERMAL CONDUCTION

In this section, we investigate the effect of anisotropic conduction on the development of the TI by performing magneto-hydrodynamics (MHD) simulations and comparing the results to hydrodynamic simulations of the TI with isotropic conduction. All of the simulations start with our fiducial density and pressure, use a conductivity $\mathcal{K} = \mathcal{K}_0$, and are computed in a domain of size 4×2 pc with our standard resolution of 2048×1024 . This means the Field length is resolved even in the cold phase with at least 3 cells.

4.1. Model parameters

We have performed a series of simulations in order to explore both the effect of varying the magnetic field geometry and strength on the nonlinear outcome of the TI. To explore the effect of geometry, we have computed models with an initially uniform magnetic field inclined along the diagonal of

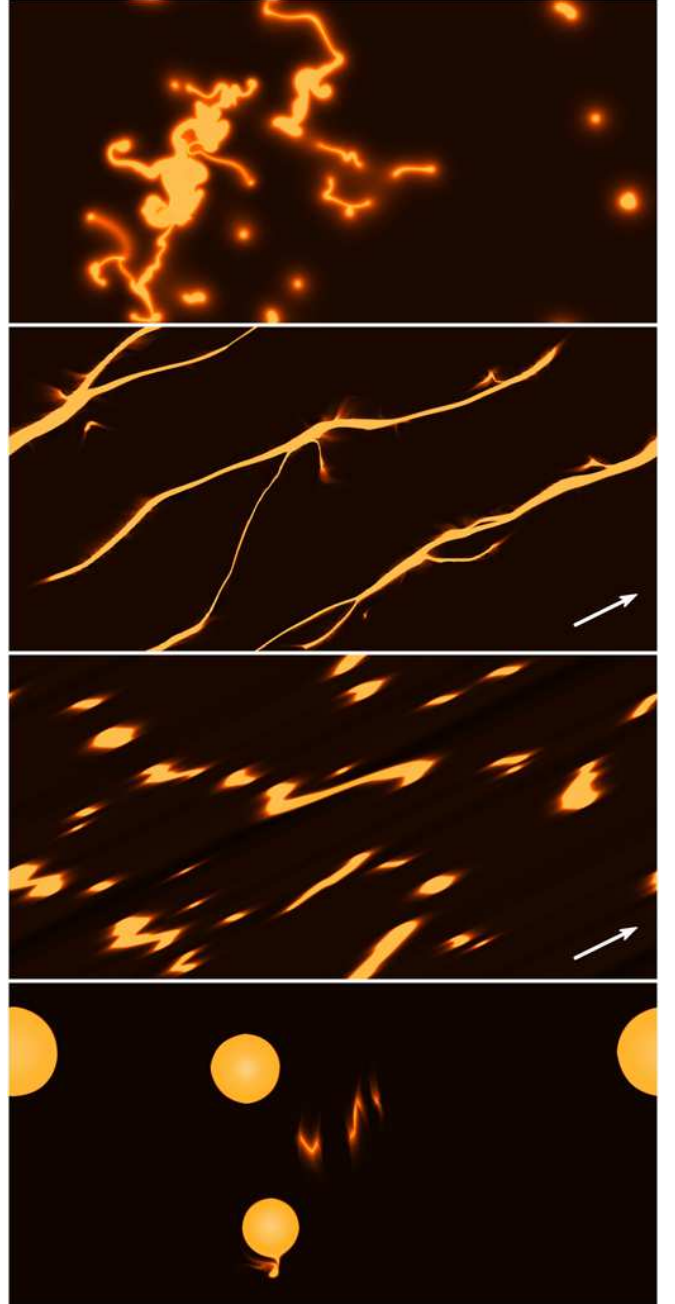


FIG. 8.— Density snapshots at $t \sim 200$ Myr in TI simulations with isotropic conduction (top), anisotropic conduction with weak uniform field (second panel), strong uniform field (third panel), and strong tangled field (bottom) respectively. The arrow shows the initial direction of the magnetic field.

the domain (to eliminate potential artifacts that might be produced by aligning the field with the grid), as well as a random tangled field generated using the technique described below. In both cases, we study two different initial magnetic field strengths corresponding to $\beta = P_{\text{gas}}/P_{\text{mag}} = [10^6, 1]$. For our fiducial initial conditions, these field strengths are $B = [0.00323, 3.23] \mu\text{G}$.

To generate the tangled magnetic field, we initialize a vector potential $\mathbf{A} = (A_x, A_y, A_z)$ which has only one non-zero component that is given by a Fourier power spectrum of the form

$$A_z = |\delta A_k| \propto k^{-11/6} \quad (15)$$

with amplitudes that follow a Gaussian random distribution

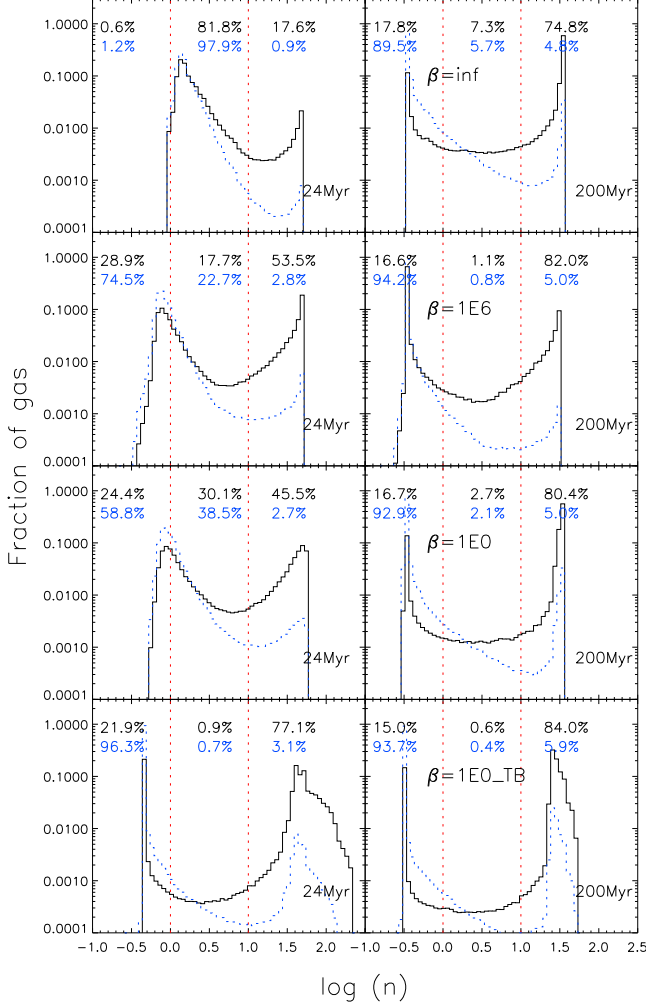


FIG. 9.— Mass (black solid line) and volume (blue dotted line) weighted density PDFs for models 6, 7, 8 and 10 at $t \sim 24$ and 200 Myr. The percentages of gas in each phase by mass are noted in black, and the proportions by volume are shown in blue.

for all wavenumbers k in the range $2\pi/(L/2) \leq k \leq 2\pi/\delta x$. The magnetic field is then $\mathbf{B} = \nabla \times \mathbf{A}$, and is normalized so that the volume averaged magnetic energy gives the appropriate value of β .

Table 2 summarizes the properties of our runs. They include two models with isotropic conduction (one with and one without viscosity), as well as 8 runs with anisotropic conduction with different magnetic field strengths and geometry. We study the TI with anisotropic conduction using both models that are inviscid, and models that include explicit viscosity with $\text{Pr} = 2/3$.

In this paper, we present four of our simulations: a hydrodynamic model with the isotropic conduction in an unmagnetized medium (Model 6) and MHD models with the anisotropic conduction in magnetized medium (Model 7, 8, and 10). For detailed study on the formation of clouds by the TI with isotropic conduction or without thermal conduction in a magnetized medium, we refer to recent papers: Hennebelle et al. (2008); Heitsch et al. (2008); Inoue & Inutsuka (2009); Banerjee et al. (2009).

4.2. Evolution of the density

Figure 8 shows snapshots of the density at $t \sim 200$ Myr from four of our simulations: a hydrodynamic model with

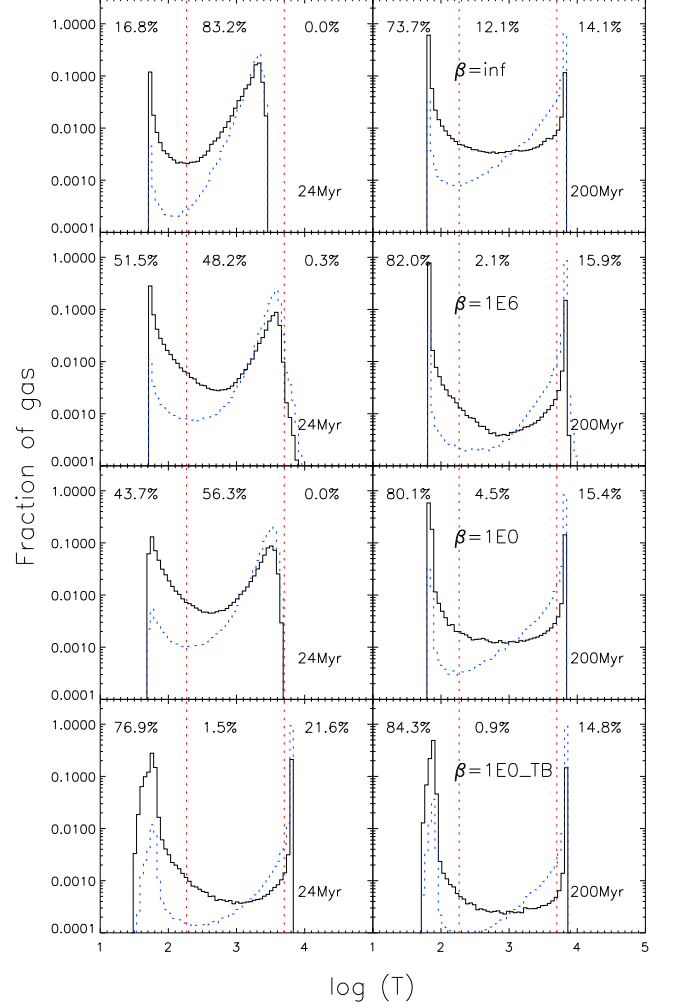


FIG. 10.— Mass (black solid line) and volume (blue dotted line) weighted temperature PDFs for models 6, 7, 8 and 10 at $t \sim 24$ and 200 Myr. The percentages of gas in each phase by mass are shown.

isotropic conduction, MHD models with anisotropic conduction and both a weak and strong uniform field, and an MHD model with anisotropic conduction and a strong tangled field. In each case, the TI results in cold regions that are more than an order of magnitude denser than their surroundings, however, the distribution and evolution of the cloud blobs are significantly different in each case.

For the hydrodynamic model with isotropic conduction (top), a network of filaments forms at about 25 Myr connecting the regions of highest density. By ~ 33 Myr, dense cold clouds begin to form. Clouds with a radius smaller than the Field length λ_F are destroyed by thermal conduction. Evaporative flows form around larger cold clouds, they are evident as the “fuzzy” edges of dense regions in Figure 8. The evaporative flows cause the dense clouds and filaments both to merge and fragment in random motions.

For the MHD model with anisotropic conduction and either a weak or strong uniform magnetic field, the regions of cooled gas tend to form thin filaments parallel to the direction of the field lines. In the linear regime, the preference for filamentation along the fields can be explained by the variation of the Field length with angle with respect to the direction of field. Perpendicular to the field, the Field length is very small, so very short wavelength perturbations are unstable. Parallel

to the field, the Field length is much longer, so only longer wavelength modes grow. As the perturbations grow nonlinear, conduction tends to enforce isothermality along magnetic field lines, leading to long filaments. In the case of strong fields, only motions along field lines are allowed, and moreover magnetic pressure provides some support in dense regions, resulting in fragments aligned with the field lines as evident in the third panel of Figure 8.

For the model with a strong tangled magnetic field (bottom panel), spherical dense clouds quickly develop at the centers of regions of closed field lines (the local minimum and maximum of the vector potential). The topology of the closed field lines in these regions means they become thermally isolated from the rest of the domain, and therefore neither evaporate nor evolve further. Small clouds originally formed in regions of open field lines eventually evaporate along the magnetic field lines and disappear.

4.3. Density and temperature statistics

Figure 9 shows the mass and volume weighted density PDFs at both 24 (left column) and 200 (right column) Myr for the four different models shown in Figure 8; from top to bottom the panels are for isotropic conduction, anisotropic conduction with weak and strong uniform field, and anisotropic conduction with a strong tangled field respectively. As was shown in section 3.1, thermal conduction can reduce the growth rate of the TI. However, models with anisotropic conduction develop density distributions with distinct peaks in the dense (cold) and diffuse (hot) phases earlier than the model with isotropic conduction. Similarly, by the end of the simulation, the hydrodynamic model with isotropic conduction has a larger amount of mass in the unstable regime compared to the models with anisotropic conduction. This interpret this result as due to the suppression of evaporative flows from the surfaces of dense clouds by the magnetic field and anisotropic conduction. As shown earlier, material in the unstable regime is contained in evaporative flows (the fuzzy edges of the clouds seen in the top panel of Figure 8). With anisotropic conduction, thermal conduction can only occur from the surfaces of the clouds where the direction of the magnetic field is normal. For the elongated and filamentary clouds formed with anisotropic conduction, only a very small fraction of its surface area is subject to evaporation, resulting in very little unstable gas. For the same reason, the fraction of high density gas (cold phase) is slightly larger in the anisotropic models compared to that of the isotropic case.

Probably the most striking feature of the density PDFs are the distinct peaks representing the two phase medium at 200 Myr. The mass and volume weighted temperature PDFs of these four models shown in Figure 10, reflect this structure: most of the matter is either in the cold or hot phases. Very little is contained in the unstable regime at intermediate temperatures, and the fraction of gas in the unstable regime decreases in the anisotropic conduction models.

4.4. Evolution of the kinetic energy

As shown in section 3.1, the TI drives evaporative flows that produce turbulence. Figure 11 compares the mass weighted mean velocity and velocity dispersion in models that include isotropic conduction, anisotropic conduction with a weak uniform field or strong uniform field, and a strong tangled field. The evolution of these quantities is a direct measure of the strength of evaporative flows.

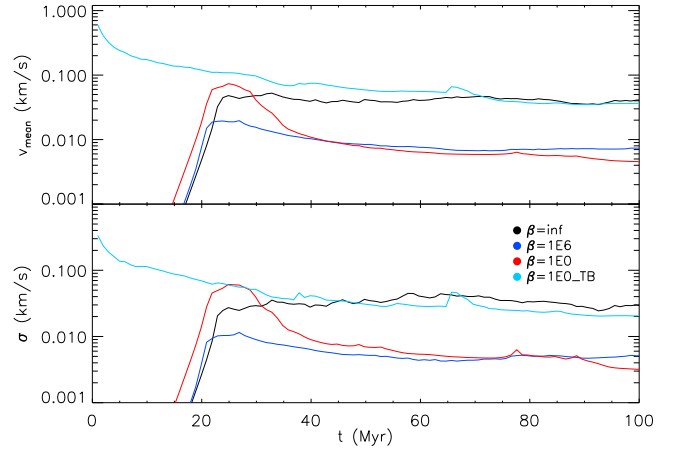


FIG. 11.— Mass weighted mean velocity (*top*) and velocity dispersion (*bottom*) as a function of time from models with hydrodynamic conduction ($\beta = \text{inf}$), 1, 6, 7, 8.

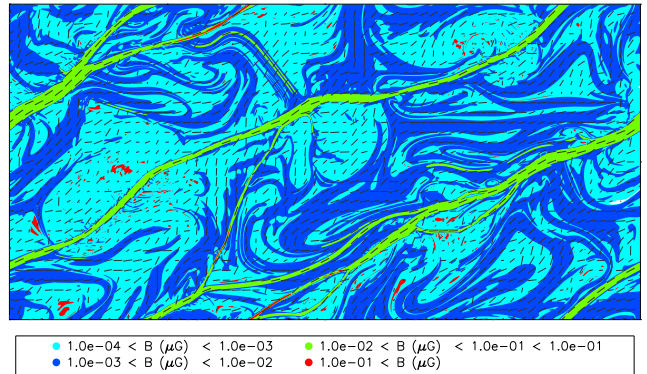


FIG. 12.— Contour plot of the magnetic field strength (color) and magnetic field lines at $t \sim 200$ Myr in TI simulation with anisotropic conduction and with weak uniform field (Model 7).

Except in the case of the tangled field, the mean velocity and dispersion grow initially, until dense clouds form and the TI saturates around 25 Myr. In the case of the strong tangled field, there are unbalanced Lorentz forces in the initial conditions that cause motions immediately. These decay away as the TI saturates. Thus, the time evolution of the velocity and its dispersion is not a good measure of TI driven turbulence in this case. For the other two models with anisotropic conduction (the strong and weak uniform field cases), the saturation amplitude of the mean velocity and dispersion at late times are about 5–10 times lower in the models with anisotropic conduction. This is clear evidence that evaporative flows from the surfaces of the dense clouds is suppressed by the magnetic field and anisotropic conduction. This is because evaporation can only occur when the field line is normal to the interface. For most of the surface of long filaments, the field is parallel to the interface. This, only a very small region at the end of the filament can produce evaporative flows.

4.5. Amplification of the magnetic field

In Figure 12, we show an image of the magnetic field strength overlaid with line segments to show the direction of the magnetic field lines at $t \sim 200$ Myr in a TI simulation with anisotropic conduction and with weak uniform field (Model 7). The magnetic field is initially uniform with a

strength of $0.00323 \mu\text{G}$. As material accumulates into the filaments by TI, the magnetic fields are compressed, resulting in strong fields that are parallel to the direction of the filament. Outside of the filaments, the magnetic field is folded and twisted by vortical fluid motions. We find the compression and twisting can amplify the field up to $0.3 \mu\text{G}$, i.e., by a factor of 100, as shown in Inoue, Inutsuka & Koyama (2007). In full three-dimensions, the geometrical compression during the formation of filaments is likely to be larger than the two-dimensional case studied here, thus the factor of 100 amplification may be a lower bound. Note the regions where the magnetic field is strongest trace the cold hydrogen filaments.

5. SUMMARY

In this work, we have studied the nonlinear regime of the thermal instability (TI) and the effect of anisotropic thermal conduction by performing two-dimensional hydrodynamical and magnetohydrodynamic simulations incorporating radiative cooling and heating. Our main results can be summarized as the following:

1. As found in previous studies, it is crucial to include explicit thermal conduction in numerical studies of the TI so that the Field length is resolved, in order to prevent artificial fragmentation driven by numerical noise at the grid scale (e.g. Figure 2).

2. The amplitude of the thermal conductivity controls the rate of evaporation from the surfaces of dense clouds formed by the TI, and therefore strongly affects the amplitude of turbulent motions induced by the TI (e.g. Figure 5).

3. Even when the Field length is resolved, explicit viscosity must be included to obtain numerical convergence of some quantities, for example the amplitude of turbulent motions driven by evaporative flows (e.g. Figure 7).

4. Although the statistics of the density and temperature are not strongly affected by anisotropic conduction, the geometry of structures formed by the TI are quite different. With anisotropic conduction and a uniform magnetic field, the TI saturates as long thin filaments of dense gas aligned with the field. In a tangled field, spherical clouds are formed in regions of closed field lines (e.g. Figure 8).

5. The combination of anisotropic conduction and MHD strongly suppresses the rate of evaporation of cold gas from the surfaces of dense structure in regions where the field is parallel to the interface. This reduces the amplitude of turbulence driven by the TI (e.g. Figure 11).

These results have a number of implications for observations of cold neutral gas in the ISM. In particular, the thin filaments along the magnetic field in the weak uniform magnetic field case agree well with recent observations of the Riegel-Crutchner cloud conducted by McClure-Griffiths et al. (2006). This neutral hydrogen (HI) cloud lies on the edge of the Local Bubble (Crutcher & Lien 1984) filled with a hot and diffuse gas where the anisotropic conduction can be expected. McClure-Griffiths et al. (2006) found a network of dozens of hairlike filaments of cold hydrogen with widths of less than ~ 0.1 pc and up to 17 pc long. They also have found that the filaments are aligned with the magnetic field of the cloud which agrees well with our results. They also calculated the magnetic field strength by using the Chandrasekhar-Fermi method, finding $\sim 60 \mu\text{G}$. We find that compression and twisting of field during the formation of filaments by the TI with anisotropic conduction can amplify it by up to a factor of 100 in two-dimensions. In three-dimensions, the amplification is likely to be larger. This may be enough to explain

the observed field.

Recently, Sharma, Parrish & Quataert (2010) have reported a study of the TI with anisotropic thermal conduction in the hot X-ray emitting plasma in clusters of galaxies. The heating and cooling processes in this regime are very different than those in the ISM studied here (equations 7 and 8 respectively), in particular there are no stable phases in the cooling curve they adopt, so that magnetic pressure sets the only limit on how cold and dense the gas becomes. Nonetheless, the structure of density condensations in this case are very similar to our results: filaments of cold gas along magnetic field lines.

Our results show that in the case of anisotropic conduction, the geometry of the magnetic field with respect to the interface between cold and hot phases is very important. Only if the field is normal to the interface can thermal conduction drive evaporation and outflows. The inclusion of anisotropic conduction could have important implications for the structure of interfaces, and the interpretation of observations of these regions (Inoue, Inutsuka & Koyama 2006; Stone & Zweibel 2009, 2010).

There are a number of limitations to our work that should be addressed in future investigations. Firstly, the ISM is highly turbulent (Heiles & Troland 2003), with typical turbulent velocities approximately 7 km s^{-1} (Heiles & Troland 2003; Mohan, Dwarakanath & Srinivasan 2004), i.e. more than 100 times larger than those produced by the TI with isotropic conduction and viscosity. In the traditional picture of the ISM, supernova driven turbulence leads to a hot, diffuse third phase (Cox & Smith 1974; McKee & Ostriker 1977). More recently, (Piontek & Ostriker 2004) have considered the interaction of turbulence driven by the MRI and TI. We have not considered the effect of externally forced turbulence on the TI in this work, however this would be a productive direction for study in the future.

Secondly, in this work we have adopted a constant conductivity \mathcal{K} . However, in reality the conductivity is a function of the temperature Parker (1953), so that the rate of thermal conduction decreases as the gas cools. The amplitude of the conductivity can vary by 2 orders of magnitude between warm and cold phases at the end of our typical simulation at $t \sim 100$ Myr. As discussed in Section 3.1, the value of the conductivity can affect the rate of evaporation from dense clouds, and therefore the kinetic energy of turbulence driven by the TI, thus assuming a constant value may alter the result. Using a realistic temperature dependent conductivity is challenging, since it would decrease the minimum value of Field length and require much higher resolution. Since the geometry of the magnetic field limits the amount of evaporation to a very small surface area at the ends of the filaments in the case of anisotropic conduction, we do not expect the use of a more realistic conductivity to produce qualitative changes in our result. Nonetheless, more realistic studies which use temperature dependent conductivities would be fruitful.

Finally, this study has considered flows in only two dimensions. In full three dimensions, the amplification of the magnetic field due to geometrical compression into filaments may be larger, and the turbulence driven by evaporative flows may be of a different character. Fully three-dimensional simulations of the TI with anisotropic conduction would also be interesting for future studies.

We thank M. Ryan Joung, Eve Ostriker, Bruce T. Draine

and Prateek Sharma for useful discussions. We thank the anonymous referee for the constructive comments. This work used computational facilities provided by the Princeton In-

stitute for Computational Science and Engineering. We acknowledge support from a grant funded through the NASA ATP.

REFERENCES

- Balbus, S. A. 2001, *ApJ*, 562, 909
 Balsara, D. S., Tilley, D. A., & Howk, J. C. 2008, *MNRAS*, 386, 627
 Banerjee, R., Vázquez-Semadeni, E., Hennebelle, P. & Klessen, R. S. 2009, *MNRAS*, 398, 1082
 Brandenburg, A., Korpi, M. J., & Mee, A. J. 2007, *ApJ*, 654, 945
 Chiéze, J. P. 1987, *A&A*, 171, 225
 Cox, D. P., & Smith, B. W. 1974, *ApJ*, 189, L105
 Crutcher, R. M., & Lien, D. J. 1984, in *IAU colloq. 81, Local Interstellar Medium*, ed. Y. Kondo, F. C. Bruhweiler, & B. D. Savage (Washington:NASA), 117
 Field, G. B. 1965 *ApJ*, 142, 531
 Field, G. B., Goldsmith, D. W., & Habing, H. J. 1969, *ApJ*, 155, 149
 Gazol, A., Sánchez-Salcedo, J., Vázquez-Semadeni, E., & Scalo, J. 2001, *ApJ*, 557, L121
 Gardiner, T. A., & Stone, J. M. 2005, *J. Comp. Phys.*, 205, 509
 Gardiner, T. A., & Stone J. M. 2008, *J. Comp. Phys.*, 227, 4123
 Heiles, C., & Troland, T. H. 2003, *ApJ*, 586, 1067
 Heitsch, R., Hartmann, L. W., Slyz, A. D., Devriendt, J. E. G., & Burkert, A. 2008, *ApJ*, 674, 316
 Hennebelle, P., & Pérault, M. 1999, *A&A*, 351, 309
 Hennebelle, P., Banerjee, R., Vázquez-Semadeni, E., Klessen, S., & Audit, E. 2008, *A&A*, 486, L43
 Inoue, T., Inutsuka, S., & Koyama, H. 2006, *ApJ*, 652, 1331
 Inoue, T., Inutsuka, S., & Koyama, H. 2007, *ApJ*, 658, L99
 Inoue, T., & Inutsuka, S. 2008, *ApJ*, 687, 303
 Inoue, T., & Inutsuka, S. 2009, *ApJ*, 704, 161
 Kim, C.-G., Kim, W., & Ostriker, E. C. 2008, *ApJ*, 681, 1148
 Koyama, H., & Inutsuka, S. 2002, 564, L97
 Koyama, H., & Inutsuka, S. 2004, 602, L25
 Koyama, H., & Inutsuka, S. 2006, *astroph/0605528*
 Kritsuk, A. G., & Norman, M. L. 2002a, *ApJ*, 569, L127
 Kritsuk, A. G., & Norman, M. L. 2002b, *ApJ*, 580, L51
 Kritsuk, A. G., & Norman, M. L. 2004, *ApJ*, 601, L55
 McClure-Griffiths, N. M., Dickey, J. M., Gaensler, B. M., Green A. J., & Haverkorn, M. 2006, *ApJ*, 652, 1339
 Mckee, C. F. & Ostriker, J. P. 1977, *ApJ*, 218, 148
 Mohan, R., Dwarakanath, K. S., & Srinivasan, G. 2004, *J. Astrophys. Astron.*, 25, 185
 Nagashima, M., Inutsuka, S., & Koyama, H. 2006, *ApJ*, 652, L41
 Parker, E. N. 1953, *ApJ*, 117, 431
 Parrish, I. J., & Stone, J. M. 2005, *ApJ*, 633, 334
 Parrish, I. J., Stone, J. M., & Lemaster, N. 2008, *ApJ*, 688, 905
 Piontek, R. A., & Ostriker, E. C. 2004, *ApJ*, 601, 905
 Piontek, R. A., & Ostriker, E. C. 2005, *ApJ*, 629, 849
 Sánchez-Salcedo, J., Vázquez-Semadeni, E., & Gazol, A. 2002, *ApJ*, 577, 768
 Sharma, P., Hammett, G., & Quataert, E. 2003, *ApJ*, 596, 1121
 Sharma, P., Quataert, E., & Stone, J. M. 2008, *MNRAS*, 389, 1815
 Sharma, P., Chandran, B. D. G., Quataert, E., & Parrish, I. J. 2009, *ApJ*, 699, 348
 Sharma, P., Parrish, I. J., & Quataert, E. 2010, *ApJ*, 720, 652
 Spitzer, L. 1958, *Rev. Mod. Phys.*, 30, 1108
 Spitzer, L. 1962, *Physics of Fully Ionized Gases* (New York: Wiley)
 Stone, J. M., Gardiner, T. A., Teuben, P., Hawley, J. F., & Simon, J. B. 2008, *ApJS*, 178, 137
 Stone, J. M., & Zweibel, E. G. 2009, *ApJ*, 696, 233
 Stone, J. M., & Zweibel, E. G. 2010, *ApJ*, 724, 131
 Vázquez-Semadeni, E., Gazol, A., & Scalo, J. 2000, *ApJ*, 540, 271
 Vázquez-Semadeni, E., Gómez, G. C., Jappsen, K., Ballesteros-Paredes, J., González, R. F., & Klessen, R. S. 2007, *ApJ*, 657, 870